Visualizing Deep Calcination of Sn Anode with Synchrotron Transmission X-Ray Microscopy

Journal:	*ACS Energy Letters*
Manuscript ID	Draft
Manuscript Type:	Letter
Date Submitted by the Author:	n/a
Complete List of Authors:	Cora, Saida; University of Massachusetts Boston, Chemistry Ge, Mingyuan; Brookhaven National Laboratory, NSLS-II Liu, Hao; Binghamton University, Department of Chemistry Briselli, Vincent; University of Massachusetts Boston Sa, Niya; University of Massachusetts Boston College of Science and Mathematics, Chemistry

Visualizing Deep Calcination of Sn Anode with Synchrotron Transmission X-Ray Microscopy

Saida Cora, Mingyuan Ge, Hao Liu, Vincent Briselli, Niya Sa*

AUTHOR INFORMATION

Corresponding Author

Niya Sa – *Department of Chemistry, University of Massachusetts – Boston, Boston, Massachusetts 02125, United States;*

Email: Niya.Sa@umb.edu

ORCID (0000-0003-4656-5851)

Authors

Saida Cora - *Department of Chemistry, University of Massachusetts – Boston, Boston, Massachusetts 02125, USA*

Email: Saida.Cora001@umb.edu

Mingyuan Ge - *National Synchrotron Light Source II (NSLS-II), Brookhaven National Laboratory, Upton, NY, 11973, USA*

Email: mingyuan@bnl.gov

Hao Liu – *Department of Chemistry, Binghamton University, Binghamton, New York 13902, USA*

Email: liuh@binghamton.edu

ORCID (0000-0003-0345-6647)

Vincent Briselli - *Department of Chemistry, University of Massachusetts – Boston, Boston, Massachusetts 02125, USA*

Email: vincent.briselli001@umb.edu

1. ABSTRACT

Ca metal anode suffers from surface passivation and struggles to effectively plate and strip in conventional Ca electrolytes, making the development of alloy anode for calcium ion battery essential. This work captures the electrochemical formation and reversibility of Ca-Sn anode with the synchrotron transmission X-ray microscopy (TXM). In particular, calciation of Sn proceeds in a core-shell manner with Ca reacting with the outer surface of Sn, leading to a distribution of Ca_xSn_y phases accompanied with the stress-induced cracking. Findings reveal the first-time report of the formation of a metastable, deep- calciated Sn phase at low electrochemical voltages. The findings offer novel insights into the phase transformations of Sn during calciation. This research contributes to the development of more robust and efficient energy storage systems, supporting the transition towards alternative battery chemistries beyond lithium-ion technology.

TOC Figure

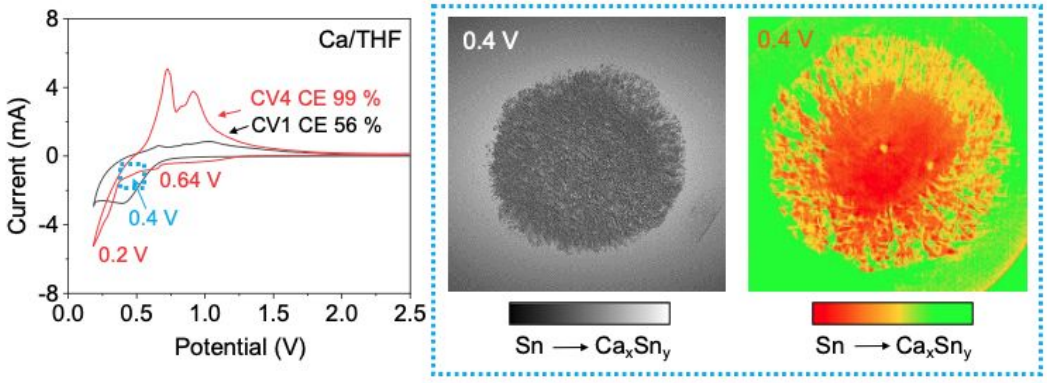

Rapid growth of the electric vehicle (EV) industry demands high-performance, cost-effective, and safe energy storage solutions. While lithium-ion batteries (LIBs) currently dominate the market, their limitations in terms of resource availability and energy density necessitate the exploration of alternative battery chemistries. Research efforts are increasingly focused on post-lithium battery systems (PLIBs) that utilize earth-abundant, environmentally benign materials.[1] Multivalent battery chemistries offer potential advantages over traditional LIBs due to their multi-electron redox capabilities, translating into a significant energy density increase.[2–4] Among the currently explored multivalent battery systems, Ca stands out as a promising contender, being the fifth most abundant element in the Earth's crust (3.63 wt% vs. 0.0065 wt% for Li), possessing a low reduction potential (–2.87 vs. Standard Hydrogen Electrode) and high volumetric capacity of 2073 mAh cm^{-3}.[5,6] However, Ca ion batteries (CIBs) face significant challenges due to the formation of an ionically insulating passivation layer on the Ca metal anode.[7–9] This significantly impacts the cycling stability of CIBs, making them impractical for real-world applications. Utilizing an alloy-type anode presents a promising avenue for enhancing the performance of CIBs, circumventing passivation issues, and improving volumetric capacity.[5,10,11] Sn has shown the ability to electrochemically alloy with Ca at a low decalciation/calciation potential of 0.53 V vs Ca.[10] The formation of the deep calcination phase Ca_2Sn, if achieved electrochemically, can deliver a theoretical capacity of 903 mAh g^{-1}.[10] Lipson *et al*. employed elemental tin as an anode paired with a manganese hexacyanoferrate (MFCN) cathode, demonstrating reversible calciation of tin in a nonaqueous electrolyte.[12] However, the cell displayed a low discharge capacity of 40 mAh/g and experienced a 50% capacity decay after 35 cycles.[12] Wang et al. demonstrated a stable room-temperature performance of CIBs using Sn foil as the anode and graphite as the cathode. This cell setup retained 95% of its capacity after 350 cycles, with Ca_7Sn_6 identified as the reversible phase.[13] In another study, a hybrid Ca-ion system was introduced, featuring a capacitor component cathode paired with a Sn foil anode.[14] This system exhibited a reversible capacity of 92 mAh g^{-1} along with good rate performance and cycle stability, maintaining a capacity retention of 84% over 1000 cycles.[14] Fichtner et al. introduced a full cell comprised of a quinone-based polymer cathode and a Ca-Sn alloy anode, which retained a capacity of 78 mAh g^{-1} relative to the organic cathode.[15] Results uncovered the transformation of dealloyed Sn into $CaSn_3$ during subsequent alloying cycles, illustrating reversible calciation/decalciation.[15]

While Sn-based Ca systems have demonstrated improvements in rate and cycling performance in CIBs, there is a need to understand and explore the electrochemical alloying mechanisms and properties of Sn anode. Many questions remain unanswered, particularly concerning the structural evolution of the Sn anode during calciation and the distribution and transformation of Sn-Ca phases within the anode. To gain deeper insights into the microstructural and chemical dynamics during the calciation/decalciation processes of Sn, this work highlights research findings that employ the synchrotron transmission X-ray microscopy (TXM, Brookhaven National Lab's beamline 18ID) to capture the electrochemical formation and reversibility of Ca-Sn phases. Supported by the detailed 3D quantitative analysis and the correlation with electrochemically discharge/charge of Sn-Ca, our findings visualize the structural and chemical

evolution within Sn particles upon reversible electrochemical calciation process. In particular, we report for the first time the formation of a metastable, deep-calcinated Sn phase at low voltages versus Ca.

Electrochemical Calciation Versus Lithiation of Sn: The comparison between the cyclic voltammetry (CV) profiles of Sn calciation versus lithiation from **Figure 1** highlights the distinct electrochemical behaviors of Sn alloy process. The Sn calciation in a 0.5 M Calcium(II) bis(trifluoromethanesulfonyl)imide ($Ca(TFSI)_2$) in tetrahydrofuran (THF) electrolyte is presented in **Figure 1a,** where the initial CV displays less pronounced redox peaks as compared to further cycles (CV #4), suggesting the activation of Sn particles. The low initial Coulombic efficiency (CE) of 56 % further suggests the structural transformations and formation of a solid electrolyte interphase (SEI) layer at the Sn interface that causes irreversible Coulombic loss. Electrochemical alloying of Sn-Ca occurs within the voltage range of 0.7 V–0.2 V vs Ca^{2+}/Ca. Specifically, peaks at 0.64 V, 0.4 V, and 0.2 V are attributed to the calciation of surface SnO, alloying of Ca with Sn, and deeper calciation leading to Ca_xSn_y phase formation, respectively. The electrochemical alloying of Sn with Ca below 0.5 V involves the formation of metastable or intermediate Ca-Sn phases, while further calciation below 0.3 V results in Ca_xSn_y phase formation. Additionally, three distinct oxidation peaks at 0.71 V, 0.84 V, and 0.91 V are attributed to the dealloying of Ca_xSn_y phases (**Figure 1a**). The increase in CE from 56% (initial CV) to 99% (CV#4) suggests good reversibility of the electrochemical alloying/dealloying of Ca_xSn_y. In contrast, the lithiation of Sn in the $LiPF_6$/EC:EMC (3:7 by wt%) presents redox peaks occurring at different voltages as compared to the Sn in Ca/THF (**Figure 1b**). A minor peak at 0.61 V on discharge is observed, corresponding to the lithiation of surface SnO and early stages of the Li–Sn alloying process (Li_xSn, $x < 1$). Notably, an increased discharge current at potentials below 0.38 V indicates the formation of the highly lithiated phases, likely $Li_{4.4}Sn$ and $Li_{2.33}Sn$, as evidenced by the broad peak at 0.3 V with peak current at 0.17 V.[16,17] This distinction in the CV profiles between the Sn cycled in Ca/THF and in $LiPF_6$/EC:EMC underscores the distinct voltage peaks associated with calciation and lithiation processes in Sn electrodes.

Ex Situ X-Ray Diffraction of Pristine and Calciated/Decalciated Sn: The diffraction pattern measured for the pristine Sn electrode exhibits intense peaks for metallic Sn at 30.7°, 32.1°, 43.9°, and 45.0°, and metallic Cu of the current collector at 43.4° (**Figure 1c**). Upon discharge of Sn to 0.2 V in the 0.5 M $Ca(TFSI)_2$/THF electrolyte, a set of new reflections (indicated by □) are observed for the calciated electrode and indicates the formation of a calciated phase. These new reflections disappear when the electrode was charged back to 2.0 V, which shows the reversible nature of the formed calciated phase. Attempts to assign these new reflections to known phases have not been successful. These new peaks do not match any of the known existing stable Sn-Ca binary phases or $CaSnO_3$ (**Figure S1-S2**).[15,18,19] The broadness of new peaks observed in the calciated Sn XRD pattern (**Figure 1c**) indicates possible structural disorder or the formation of small domains of Sn-Ca. It is possible that this unknown phase is metastable and only formed

electrochemically. Nevertheless, the XRD data provide direct evidence for the reversible formation of a crystalline phase during electrochemical decalciation of the Sn powder.

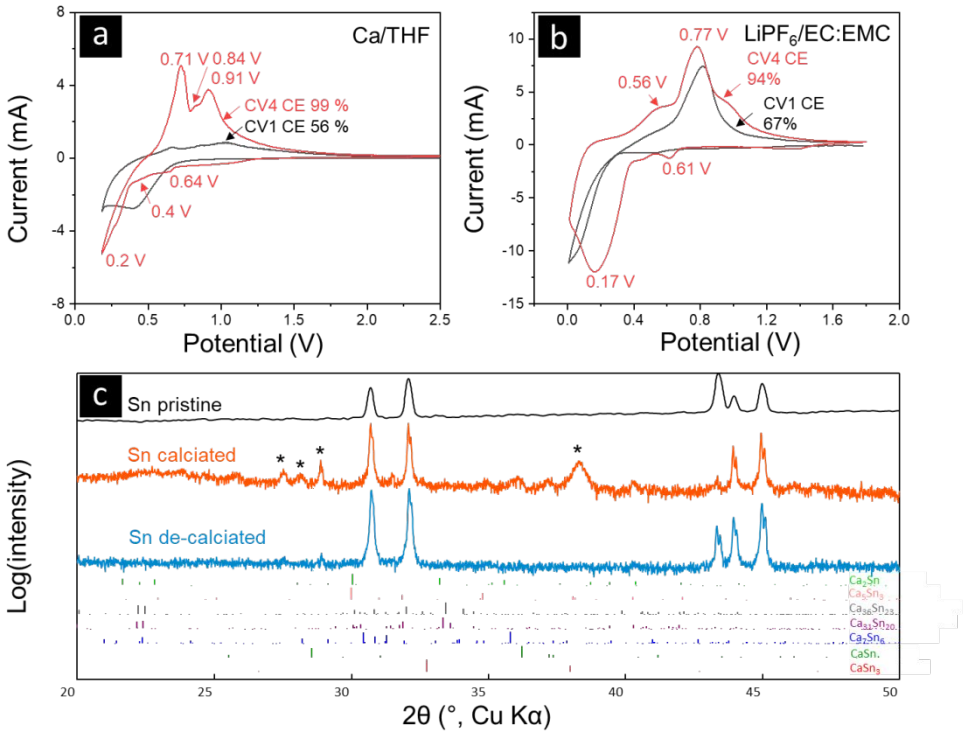

Figure 1. (a) Representative cyclic voltammetry (1st and the 4th cycle) with Sn as WE and Li as RE/CE in a 3-electrode Swagelok cell. A 0.5 M $Ca(TFSI)_2$ in THF is used as electrolyte, voltage is scanned from 2.5 V to 0.2 V at 0.001 V/s; **(b)** Representative cyclic voltammetry (1st and the 4th cycle) with the same electrochemical cell setup in a 1.2 M $LiPF_6$/EC:EMC electrolyte. Voltage is scanned from 1.8 V to 0.005 V at 0.001 V/s. Coulombic efficiencies (CE) are presented on the CV curves; **(c)** Ex situ XRD of the pristine Sn laminate, discharged (0.2 V, orange) Sn in a 0.5 M $Ca(TFSI)_2$ in THF electrolyte, and charged Sn (2.0 V, blue). The symbol "*" indicates the new peaks appearing upon discharge. Intensities are plotted on a logarithmic scale.

Imaging and Elemental Mapping of the Electrochemically Alloying of Sn and Ca: The SEM images in **Figure 2** reveal morphological changes in the Sn laminate electrode upon discharge (calciation) in the Ca electrolyte. The SEM in **Figure 2a** shows pristine Sn laminate, which is comprised of spherical Sn particles embedded within a laminate coating containing carbon powder and PVDF binder. These spherical particles feature smooth morphology, free of cracks, and are evenly distributed across the electrode surface. In contrast, the discharged (calciated) Sn electrode in **Figure 2b** shows a rougher surface morphology with particles featuring cracks caused by the formation of Ca_xSn_y phases at 0.4 V. The Sn particles appear larger, suggesting that the calciation process induces volume changes within the electrode material, leading to the formation of cracks

and increased porosity. The presence of cracks could be attributed to the reactions between Sn and Ca during calciation, resulting in the formation of Ca_xSn_y phases, as observed in the XRD spectra in **Figure 1c**. The formation of these new phases could lead to stress within the electrode material, causing the observed cracking. Additionally, the volume changes associated with the phase transformations during calciation could contribute to the formation of cracks. The EDS analysis of the calciated Sn in **Figure 2c** provides insights into the elemental composition. The observation of Sn, O, and Ca is consistent with the existence of tin, tin oxides, and calciated tin phases. The observed spatial distribution of the Ca and Sn elemental signals suggests alloying of Ca within Sn particles.

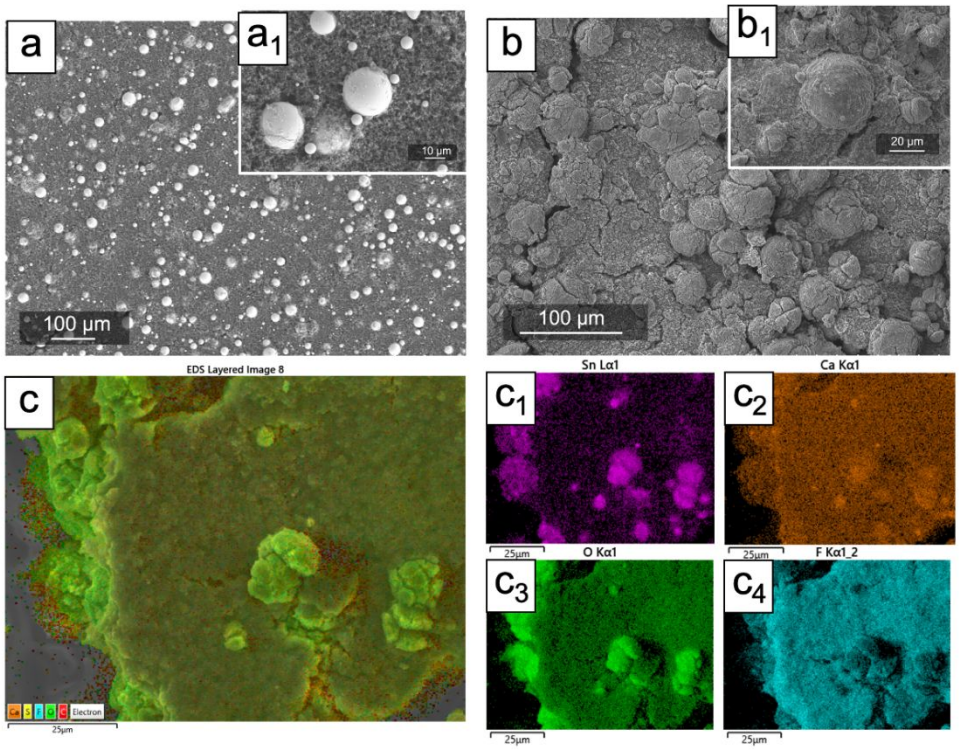

Figure 2. SEM images of (a & a_1) pristine Sn laminate; (b & b_1) Sn laminate cycled for 6 CVs and discharged to 0.4 V in $Ca(TFSI)_2$ electrolyte; (c & $c_1 - c_4$) EDS of Sn laminate discharged to 0.4 V in $Ca(TFSI)_2$ electrolyte showing the distribution of Sn, Ca, O, and F elements. The electrochemical cycling was performed in the Swagelok cell with Sn laminate as WE and Li metal as RE/CE in the potential window from 2.5 V to 0.2 V at 0.001 V/s; after 6 CVs, the cell was discharged to 0.4 V at a constant current of -40 µA.

Void-to-Particle Area of Calciated Sn: **Figure 3** depicts the virtual slices of the reconstructed Sn particles obtained through X-Ray tomography of pristine Sn particle and calciated Sn discharged in 0.5 M $Ca(TFSI)_2$ in THF at 0.6 V, 0.4 V, and 0.2 V. These images reveal a strong correlation between the calciation stage and its morphological evolution such as the crack formation and volume expansion. The pristine Sn particles are initially spherical and crack-free (i.e., no void);

however, decreasing discharge voltage from 0.6 V to 0.2 V drives the formation of Ca_xSn_y phases, where the void-to-particle area ratio progressively increased from 14% at 0.6 V to 25% at 0.4 V, and 45% at 0.2 V (**Figure 3e)**. The Sn-Ca alloy formation starts from the Sn particles' outer surface and propagates into the particle's interior, which is supported by the core-shell mechanism. The crack-free core observed at the initial calciation voltage of 0.6 V (**Figures. 3b&f**) and the intermediate voltage of 0.4 V (**Figures. 3c&g**) suggests a gradual stress gradient within the Sn particle. At the lowest voltage of 0.2 V (**Figures. 3d&e**), extensive cracking throughout the whole particle is observed with a significant increase of the void-to-particle ratio to 45% (*versus* 14% at 0.6 V), corresponding the disintegration of the entire Sn particle by stress-driven crack propagation. Additional cross-section virtual slices of calciated and decalciated Sn particles are presented in **Figures S3 and S4** and show similar trend. These findings reveal the critical effect of calciation on the structural integrity of Sn particles during discharge in Ca electrolyte.

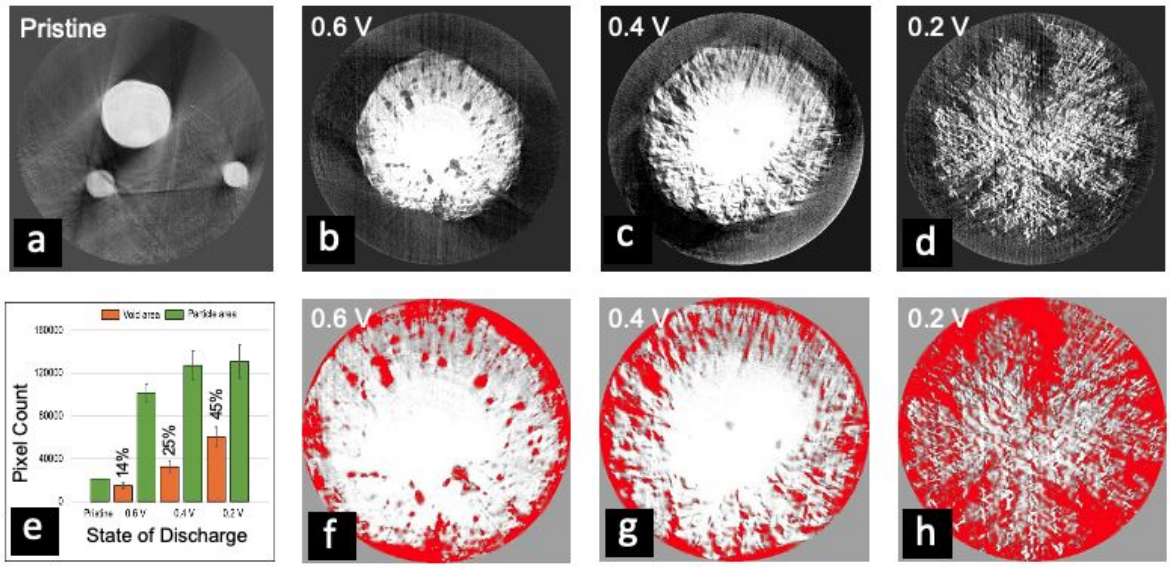

Figure 3. (a) Ex situ X-Ray tomography of Sn particles. A cross-section of (a) pristine and discharged Sn in a 0.5 M $Ca(TFSI)_2$ in THF electrolyte at (b) 0.6 V, (c) 0.4 V, (d) 0.2 V; (e) Void-to-particle area ratio based on the analysis of multiple particles (>5) from each discharge state; (f-h) Void-to-particle area with color contrast indicating the area of the voids (red) for calciated Sn particle at the corresponding state of discharge.

Phase Distribution of the Electrochemically Alloying of Sn and Ca: The transition from pristine Sn particle to calciated Sn unveils a distinctive core-shell architecture as seen in **Figure 4**. The false-colored orange core signifies pristine Sn (**Figure 4e**), while the green color in **Figure 4f-h** denotes the formation of Ca_xSn_y phases. A green Ca_xSn_y phase forms around the remaining orange

Sn core. This distinct color difference suggests a core-shell morphology, where calciation progresses from the outer surface inwards, suggesting that Ca ions readily react with Sn on the outer surface, forming Ca_xSn_y. This discernible core-shell morphology suggests a non-uniform and a heterogeneous spatial distribution of phases arising from the alloying process between Ca and Sn at discharge. The concurrent cracking and fragmentation propagating from the green shell toward the orange core, is attributed to the large lattice mismatch at the reaction front between the surface Ca_xSn_y phases and unreacted Sn core, which induces stress within the particle and ultimately leads to stress-induced cracking.[20–23]

The chemical compositional change can be characterized by the linear attenuation coefficient, which is dictated by the material's composition and mass density.[24] The attenuation coefficient is expected to decrease linearly with Ca atomic fraction for the Ca-Sn binary phases (**Table S1 and Figure S5**). **Figure 5** shows the histogram of the attenuation coefficient of all voxels in the reconstructed models for the pristine Sn electrode and calciated electrodes discharged to 0.6 V, 0.4 V, and 0.2 V. These voltages correspond to the distinct discharge stages characterized by the CV peaks in **Figure 1a**. The histogram shows a bimodal distribution of the attenuation coefficients for all samples being investigated: one mode centers around zero and is attributed to the less absorbing phases that include carbon black, binder, and electrolyte; the other mode centers at a higher attenuation coefficient and is attributed to the more absorbing phases of Sn and Ca_xSn_y. For the pristine Sn electrode, the attenuation coefficient for pure Sn particles is centered at 0.182 μm^{-1}. Upon discharge to 0.6 V, the Sn attenuation coefficient peak disappears while a new peak emerges at 0.125 μm^{-1} (equal to 70% of the voxel value of pure Sn). It must be noted that the measured attenuation coefficient only corresponds to the lower bound for a specific phase because voids smaller than the dimension of the voxel/pixel cannot be resolved. Therefore, this peak at 0.125 μm^{-1} is consistent with the formation of the $CaSn_3$ phase, whose attenuation coefficient is 80% of that for pure Sn. The attenuation coefficient for the more absorbing phase(s) shifts to 0.106 μm^{-1} at 0.4 V, which can be attributed to the further calciation of multiple Ca_xSn_y phases with a higher Ca concentration than $CaSn_3$. It is worth noting that the discharged state at 0.2 V results in the complete disappearance of the Sn peak and the appearance of a new peak at 0.053 μm^{-1} (equal to 30% of the attenuation coefficient of pure Sn), possibly attributed to the fully calciated Ca_2Sn phase. The attenuation coefficient for Ca_2Sn is 40% of Sn and is consistent with this new peak at 0.053 μm^{-1}. The newly formed Bragg peaks for the electrode discharged to 0.2 V do not match any known stable Ca_xSn_y phases, therefore, such fully calciated phase is likely to be metastable. Upon decalciation, the particle undergoes a reconstructive transformation (**Figure S3)**. This transformation can involve the reorganization of the Sn atoms as the calcium ions are extracted, potentially leading to a healing process where the Sn structure attempts to revert to its original or a new stable form. However, the decalciated Sn particle has a porous interior due to the incomplete return to the pristine state leading to residual voids. A similar self-healing process was observed during the initial desodiation of Sn, where despite significant volume shrinkage, negligible structural pulverization or damage was observed after the first Na-ion extraction.[21] In contrast, in

analogous LIB with Sn anode, mechanical degradation with drastic morphology changes occurred mainly during the first delithiation process, not the first lithiation. These structural changes and self-healing during the initial calciation-decalciation of Sn may favor the microstructural stability in subsequent electrochemical cycles.

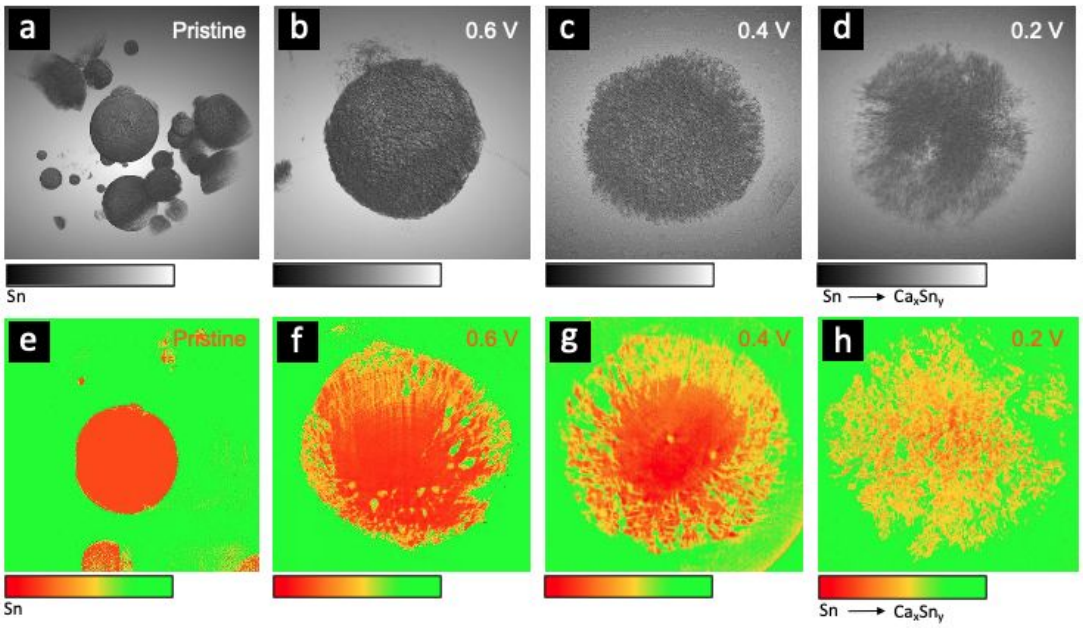

Figure 4. (a-b) X-Ray Tomography with 3D view of (a) pristine Sn; (b) calciated Sn at 0.6 V, (c) calciated Sn at 0.4 V, (d) calciated Sn at 0.2 V; (e-h) False colored cross-section images of pristine Sn and Sn calciated at 0.6 V, 0.4 V, and 0.2 V voltage states to show Ca_xSn_y phases and their distribution within Sn particle.

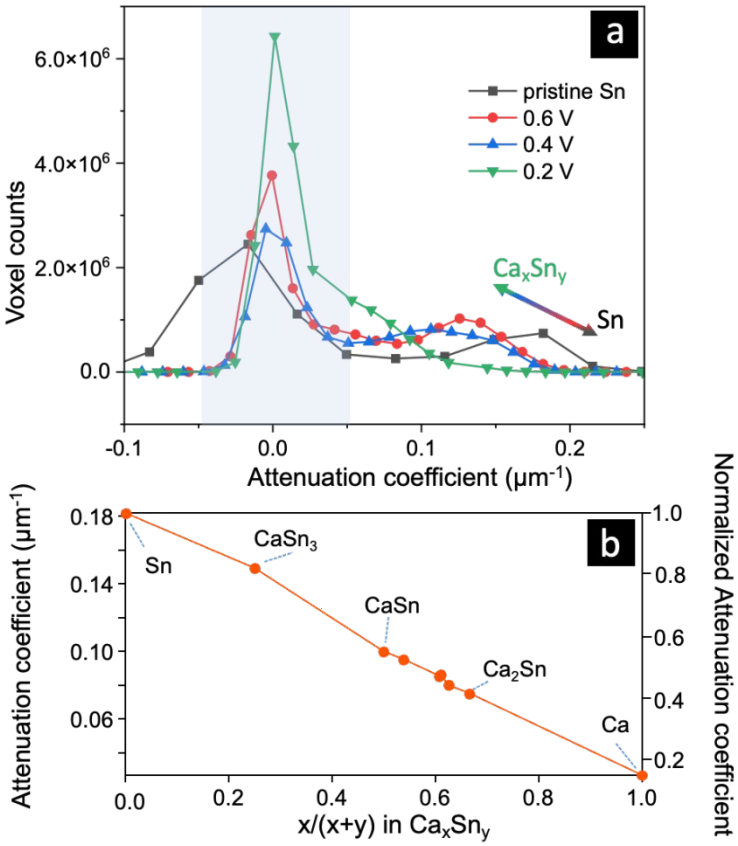

Figure 5. (a) X-ray attenuation coefficient histograms during electrochemical calciation of Sn; (b) simulated attenuation coefficient for various Ca-Sn phases.

The investigation into the electrochemical behavior and structural and phase evolution of Sn electrodes during calciation/decalciation processes offers new and exciting insights into the intricate mechanisms underlying Sn-based CIB systems. First, the confirmation of reversible alloying/dealloying processes involving Sn and Ca is reported, providing crucial evidence of the practical applicability of Sn-based anode as a viable material for high-performance and environmentally friendly Ca-based battery systems. The transformation of Sn electrodes into calciated Sn upon deep discharge, evidenced by ex-situ X-ray diffraction and X-ray tomography, highlights the formation of new metastable phases with a higher calciation level than $CaSn_3$. Applying ex-situ X-ray nanotomography to visually and quantitatively understand the structural changes and phase distribution during calciation of Sn presents a novel approach that is less documented in current studies, particularly within CIB systems. Nanotomography analysis reveals the transformation of Sn electrodes into highly calciated Ca_xSn_y ($x/y > 1/3$) phases upon deep

discharge, complemented by insights into how specific alloy phases formed at various discharge stages contribute to structural evolution and the stress-induced formation of cracks within Sn. Chemical analysis using X-ray attenuation coefficients quantitatively measures the extent of calciation, providing new and previously unreported insights into the phase transformations in the calciation process of Sn particles. Using 3D quantitative analysis and linking it with the discharge/charge of Sn in Ca/THF electrolyte, this research demonstrates a detailed structural and chemical evolution of Sn particles upon calciation, highlighting the electrochemical reversibility of the development of improved Ca-ion batteries with Sn anode.

EXPERIMENTAL METHODS

Electrode and Electrolyte Preparation: Sn electrodes were prepared by mixing as-received Sn powder (20 μm, >99.95%, US Research Nanomaterials, Inc.) with 12% polyvinylidene fluoride (PVDF) in 1-methyl 2- pyrrolidinone (NMP, Sigma Aldrich) and carbon black (Timical) at a weight ratio of 80:10:10 to make a slurry. The slurry was coated on a Cu foil current collector (thickness: ~9 μm) and carbon paper by a doctor blade method and then dried overnight in an oven at 110 °C under vacuum. The resulting laminate had a thickness of 100 μm. The electrolyte solution was prepared from 0.5 M Calcium(II) bis(trifluoromethylsulfonyl)imide ($Ca(TFSI)_2$, Solvionic, France) dried overnight in the vacuum oven (Buchi, Sweden) at 150^o C and dissolved in a tetrahydrofuran solvent (THF, Sigma Aldrich). The Gen2 electrolyte (1.2 M $LiPF_6$ in 3:7 by weight ethylene carbonate (EC) and ethyl methyl carbonate (EMC)) was used as received (Tomiyama High Purity Chemical Industries Ltd, Japan).

***Electrochemical Testing*:** A Swagelok half-cell was assembled using the Sn electrode as a working electrode, a glass fiber separator (GF/A, Whatman), and a Li metal (99.9%, Goodfellow) as a counter and reference electrode in an Ar-filled glovebox (Vacuum Technology Inc.) with H_2O and O_2 under 0.1 ppm. The electrochemical cyclic voltammetry was conducted in the voltage window from 2.5 V to 0.2 V (vs Li/Li^+) at a scan rate of 1 mV/s and controlled by the Potentiostat (Princeton Applied Instruments). The charge/discharge was performed at a constant current of 40 μA until the cell was discharged to voltages of 0.6 V, 0.4 V, and 0.2 V and charged to 2.0 V. Data acquisition for the electrochemical measurements was performed using Versa studio.

***Transmission X-Ray Microscopy (TXM)*:** Ex situ X-ray nanotomography was performed using full-field transmission X-ray microscopy (TXM) at beamline 18ID at the National Synchrotron Light Source II (NSLS II) at Brookhaven National Lab (BNL). For each electrochemical calciated-decalciated Sn, a nanotomography data set was collected with 8 keV X-rays, using 540 projections over an angular range of 180° with a field of view of 40 × 40 μm. The pixel size was 40 ×

40 nm. The tomography of 15-20 particles was collected from each Sn anode sample, and statistics were taken. Histogram calculation and normalization of attenuation coefficients were performed as adapted from previously reported studies.[24] Following reconstruction, the resulting tomograms provided 3D grayscale images, where each voxel's grayscale value (ω) represents the relative X-ray attenuation at that location. To extract absolute attenuation coefficients (μ), histograms were generated from selected regions of interest (ROIs) containing both Sn particles (or calciated Sn particles) and the background containing carbon black and binder. The histograms captured the grayscale distribution within the ROI and displayed two distinct peaks: one corresponding to the high-attenuation Sn phase and the other to the low-attenuation carbon-rich background. Theoretical attenuation coefficients were calculated using known mass attenuation coefficients and material densities,[25] with elemental Sn representing the Sn phase and elemental carbon used as an approximation for the background. These calculated values were then assigned to the grayscale peak positions in the histogram. With these two reference points - grayscale value and attenuation coefficient - a linear normalization function was derived:

$$\mu(\omega) = a\omega + b$$

with $a = 13.051\ \mu m^{-1}$ and $b = 0.0082\ \mu m^{-1}$. The normalization function enabled the conversion of grayscale values throughout the tomograms into absolute attenuation coefficients, allowing for quantitative analysis of material composition.

***X-ray Diffraction (XRD) and Scanning Electron Microscopy (SEM)/Energy-Dispersive X-Ray Spectroscopy (EDS) Analysis*:** The surface morphology and chemical mapping analysis of the Sn electrodes before and after electrochemical charge/discharge was performed with a field emission scanning electron microscope (FESEM, ZEISS Sigma 500, Germany) at an acceleration voltage of 5-10 kV. Sn anode was discharged in a 2-electrode Swagelok cell with a 0.5 M Calcium(II) bis(trifluoromethanesulfonyl)imide ($Ca(TFSI)_2$) in tetrahydrofuran (THF) electrolyte and held at 0.2 V vs Li^+/Li for 1 hr. The elemental analyses were conducted with the SEM equipped with an energy-dispersive X-ray spectroscopy detector (EDS, Oxford Instruments, UK) at the acceleration voltage of 15 kV with the data analysis performed by the AZtec software package (Oxford Instruments, UK). X-ray diffraction (XRD) patterns of pristine Sn and Sn discharged in Ca/THF electrolyte to 0.2 V were recorded using a Rigaku X-ray diffractometer (Rigaku, Japan) with Cu Kα radiation. The scan range was from 10° to 80° 2θ. The XRD spectra was analyzed using the SmartLab Software.

Supporting Information Available: tabulated X-ray absorption lengths and attenuation coefficients for stable Sn-Ca binary phases, additional XRD patterns for all known stable Ca-Sn binary phases at room temperature and simulated Bragg positions for polymorphs of $CaSnO_3$.

Author Information:

Notes: The authors declare no competing financial interests.

Acknowledgements:

This work is financially supported by the NSF CAREER grant (Grant No. 2047753). Author Saida Cora is fully sponsored by the U.S. Department of Energy, Office of Science, Office of Workforce Development for Teachers and Scientists, Office of Science Graduate Student Research (SCGSR) program. The SCGSR program is administered by the Oak Ridge Institute for Science and Education (ORISE) for the DOE. ORISE is managed by ORAU under contract number DE-SC0014664. This research used resources at the NSLS-II beamline of the National Synchrotron Light Source, a U.S. Department of Energy (DOE) Office of Science User Facility operated for the DOE Office of Science by Brookhaven National Laboratory under Contract No. DE-SC0012704. The US Government retains and the publisher, by accepting the article for publication, acknowledges that the US Government retains a non-exclusive, paid-up, irrevocable, worldwide license to publish or reproduce the published form of this work, or allow others to do so, for US Government purposes. All opinions expressed in this paper are the author's and do not necessarily reflect the policies and views of DOE, ORAU, or ORISE. N.S. would like to acknowledge the Proposal Development Grant from the University of Massachusetts Boston. Acquisition of the advanced FESEM is acknowledged from the MRI grant of the National Science Foundation (Grant No. 1919919).

6. REFERENCES

(1) Ponrouch, A.; Palacín, M. R. Post-Li Batteries: Promises and Challenges. *Philos Trans A Math Phys Eng Sci* **2019**, *377* (2152), 20180297. https://doi.org/10.1098/rsta.2018.0297.

(2) Liang, Y.; Dong, H.; Aurbach, D.; Yao, Y. Current Status and Future Directions of Multivalent Metal-Ion Batteries. *Nat Energy* **2020**, *5* (9), 646–656. https://doi.org/10.1038/s41560-020-0655-0.

(3) Xu, C.; Chen, Y.; Shi, S.; Li, J.; Kang, F.; Su, D. Secondary Batteries with Multivalent Ions for Energy Storage. *Sci Rep* **2015**, *5*, 14120. https://doi.org/10.1038/srep14120.

(4) Chen, R.; Luo, R.; Huang, Y.; Wu, F.; Li, L. Advanced High Energy Density Secondary Batteries with Multi-Electron Reaction Materials. *Advanced Science* **2016**, *3* (10), 1600051. https://doi.org/10.1002/advs.201600051.

(5) Tinker, H. R.; Howard, C. A.; Zhou, M.; Xu, Y. Exploring Anodes for Calcium-Ion Batteries. *Mater. Adv.* **2023**, *4* (9), 2028–2041. https://doi.org/10.1039/D2MA01034H.

(6) Hosein, I. D. The Promise of Calcium Batteries: Open Perspectives and Fair Comparisons. *ACS Energy Lett.* **2021**, *6* (4), 1560–1565. https://doi.org/10.1021/acsenergylett.1c00593.

(7) Zhao, Y.; Wang, A.; Ren, L.; Liu, X.; Luo, J. Revealing the Solid Electrolyte Interface on Calcium Metal Anodes. *Journal of Energy Chemistry* **2022**, *70*, 174–190. https://doi.org/10.1016/j.jechem.2022.02.022.
(8) Forero-Saboya, J.; Davoisne, C.; Dedryvère, R.; Yousef, I.; Canepa, P.; Ponrouch, A. Understanding the Nature of the Passivation Layer Enabling Reversible Calcium Plating. *Energy Environ. Sci.* **2020**, *13* (10), 3423–3431. https://doi.org/10.1039/D0EE02347G.
(9) Wei, Q.; Zhang, L.; Sun, X.; Liu, T. L. Progress and Prospects of Electrolyte Chemistry of Calcium Batteries. *Chem. Sci.* **2022**, *13* (20), 5797–5812. https://doi.org/10.1039/D2SC00267A.
(10) Yao, Z.; Hegde, V. I.; Aspuru-Guzik, A.; Wolverton, C. Discovery of Calcium-Metal Alloy Anodes for Reversible Ca-Ion Batteries. *Advanced Energy Materials* **2019**, *9* (9), 1802994. https://doi.org/10.1002/aenm.201802994.
(11) Deng, X.; Li, L.; Zhang, G.; Zhao, X.; Hao, J.; Han, C.; Li, B. Anode Chemistry in Calcium Ion Batteries: A Review. *Energy Storage Materials* **2022**, *53*, 467–481. https://doi.org/10.1016/j.ensm.2022.09.033.
(12) Lipson, A. L.; Pan, B.; Lapidus, S. H.; Liao, C.; Vaughey, J. T.; Ingram, B. J. Rechargeable Ca-Ion Batteries: A New Energy Storage System. *Chem. Mater.* **2015**, *27* (24), 8442–8447. https://doi.org/10.1021/acs.chemmater.5b04027.
(13) Wang, M.; Jiang, C.; Zhang, S.; Song, X.; Tang, Y.; Cheng, H.-M. Reversible Calcium Alloying Enables a Practical Room-Temperature Rechargeable Calcium-Ion Battery with a High Discharge Voltage. *Nature Chem* **2018**, *10* (6), 667–672. https://doi.org/10.1038/s41557-018-0045-4.
(14) Wu, N.; Yao, W.; Song, X.; Zhang, G.; Chen, B.; Yang, J.; Tang, Y. A Calcium-Ion Hybrid Energy Storage Device with High Capacity and Long Cycling Life under Room Temperature. *Advanced Energy Materials* **2019**, *9* (16), 1803865. https://doi.org/10.1002/aenm.201803865.
(15) Zhao-Karger, Z.; Xiu, Y.; Li, Z.; Reupert, A.; Smok, T.; Fichtner, M. Calcium-Tin Alloys as Anodes for Rechargeable Non-Aqueous Calcium-Ion Batteries at Room Temperature. *Nat Commun* **2022**, *13* (1), 3849. https://doi.org/10.1038/s41467-022-31261-z.
(16) Lucas, I. T.; Pollak, E.; Kostecki, R. *In Situ* AFM Studies of SEI Formation at a Sn Electrode. *Electrochemistry Communications* **2009**, *11* (11), 2157–2160. https://doi.org/10.1016/j.elecom.2009.09.019.
(17) Yang, Z.; Dixon, M. C.; Erck, R. A.; Trahey, L. Quantification of the Mass and Viscoelasticity of Interfacial Films on Tin Anodes Using EQCM-D. *ACS Appl. Mater. Interfaces* **2015**, *7* (48), 26585–26594. https://doi.org/10.1021/acsami.5b07966.
(18) Palenzona, A.; Manfrinetti, P.; Fornasini, M. L. Phase Diagram of the Ca–Sn System. *Journal of Alloys and Compounds* **2000**, *312* (1), 165–171. https://doi.org/10.1016/S0925-8388(00)01150-6.
(19) Amalraj, A.; Pavadai, R.; Perumal, P. Recyclable Target Metal-Enhanced Fluorometric Naked Eye Aptasensor for the Detection of Pb2+ and Ag+ Ions Based on the Structural Change of CaSnO3@PDANS-Constrained GC-Rich ssDNA. *ACS Omega* **2021**, *6* (45), 30580–30597. https://doi.org/10.1021/acsomega.1c04319.
(20) Brandt, L. R.; Marie, J.-J.; Moxham, T.; Förstermann, D. P.; Salvati, E.; Besnard, C.; Papadaki, C.; Wang, Z.; Bruce, P. G.; Korsunsky, A. M. Synchrotron X-Ray Quantitative Evaluation of Transient Deformation and Damage Phenomena in a Single Nickel-Rich

Cathode Particle. *Energy Environ. Sci.* **2020**, *13* (10), 3556–3566. https://doi.org/10.1039/D0EE02290J.

(21) Wang, J.; Eng, C.; Chen-Wiegart, Y. K.; Wang, J. Probing Three-Dimensional Sodiation–Desodiation Equilibrium in Sodium-Ion Batteries by in Situ Hard X-Ray Nanotomography. *Nat Commun* **2015**, *6* (1), 7496. https://doi.org/10.1038/ncomms8496.

(22) Lim, C.; Yan, B.; Yin, L.; Zhu, L. Simulation of Diffusion-Induced Stress Using Reconstructed Electrodes Particle Structures Generated by Micro/Nano-CT. *Electrochimica Acta* **2012**, *75*, 279–287. https://doi.org/10.1016/j.electacta.2012.04.120.

(23) Zhang, X.; Shyy, W.; Sastry, A. M. Numerical Simulation of Intercalation-Induced Stress in Li-Ion Battery Electrode Particles. *J. Electrochem. Soc.* **2007**, *154* (10), A910. https://doi.org/10.1149/1.2759840.

(24) Ebner, M.; Marone, F.; Stampanoni, M.; Wood, V. Visualization and Quantification of Electrochemical and Mechanical Degradation in Li Ion Batteries. *Science* **2013**, *342* (6159), 716–720. https://doi.org/10.1126/science.1241882.

(25) Hubbell, J. H.; Seltzer, S. M. X-Ray Mass Attenuation Coefficients. *NIST* **2009**, *NIST Standard Reference Database 126*. https://doi.org/10.18434/T4D01F.